









Cite this: *Phys. Chem. Chem. Phys.*,
2025, 27, 5909

Building a cost-effective mechanochemical Raman system: improved spectral and time resolution for *in situ* reaction and rheology monitoring†

Goran Zgrablić, ^a Ana Senkić, ^a Noa Vidović, ^b Krunoslav Užarević, ^c
Davor Čapeta, ^{*a} Ivana Brekalo ^{*c} and Mario Rakić ^a

Raman spectroscopy has become an indispensable tool for *in operando* monitoring in preparative mechanochemistry due to its ability to provide real-time, non-invasive insight into solid-state reactions. While commercial systems based on fiber Raman probes offer ease of use and plug-and-play deployment, their relatively low spectral resolution and lower sensitivity make them less suitable for the specific demands of mechanochemical reaction monitoring. To address these challenges and make this valuable methodology widely available, we describe a high-sensitivity free-optics Raman system, termed mcRS (mechanochemical Raman System), constructed from the ground up using affordable off-the-shelf optical components. The mcRS includes a free-space Raman probe and a custom-designed dispersive spectrometer utilising only lenses, paired with a low-cost industrial-grade CMOS camera as the detector. By fine-tuning the optics to minimise photon loss and achieving tighter spot sizes on the detector, the mcRS provides a 30% improvement in spectral resolution compared to previous in-house fiber-based systems for half of the cost and offers a five-fold reduction in price compared to commercial systems. This is accompanied by a five-fold improvement in time resolution and a novel feature, the possibility to simultaneously collect Raman data and monitor the rheology of the sample, which often plays an important role in mechanochemical reactions. We validated the mcRS performance by monitoring the reaction between ZnO and imidazole under neat grinding (NG) and liquid-assisted grinding (LAG) conditions, using ethanol as the liquid additive. The enhanced capabilities of the mcRS offer significant advancements in the *in situ* studies of mechanochemical processes, allowing for differentiation between two zeolitic imidazolate framework products based on subtle differences in the high-frequency modes (3100–3200 cm⁻¹).

Received 17th December 2024,
Accepted 23rd February 2025

DOI: 10.1039/d4cp04757e

rsc.li/pccp

Introduction

Mechanochemical reactivity, the initiation of chemical reactions by mechanical force, attracts significant attention in materials science and has become one of the main synthetic tools of Green Chemistry.¹ Mechanochemical synthetic procedures are highly advantageous compared to traditional solvothermal synthesis as they are fast, scalable, atom economic, do not require the extensive use of solvents or large amounts of

energy, and often result in quantitative conversion with little to no waste generated. Mechanochemical synthesis is now applied to almost all areas of chemical synthesis^{2–10} and can sometimes provide the only synthetic pathways to access otherwise unstable solid phases and composite materials.^{11–14} The synthetic potential of mechanochemistry can also be significantly expanded by combining mechanical action with different energy inputs such as heat, light, electricity or sound, affording new levels of solid-state reactivity.¹⁵ Due to all these reasons, in 2019 mechanochemistry was named by IUPAC as one of ten innovations that will change the world.¹⁶

Two major breakthroughs in the development of mechanochemistry largely enabled its current utility and versatility: the use of additives and the introduction of *in situ* monitoring techniques. Adding small amounts of liquids,^{17,18} polymers,^{19,20} ionic salts,²¹ and non-ionic solid additives²² has been shown to greatly accelerate mechanochemical reactions and change their

^a Institute of Physics, Bijenička 46, 10000 Zagreb, Croatia. E-mail: dcapeta@ifs.hr

^b Department of Physics, Faculty of Science, University of Zagreb, Bijenička 32, 10000 Zagreb, Croatia

^c Ruđer Bošković Institute, Bijenička 54, 10000 Zagreb, Croatia.

E-mail: ibrekalo@irb.hr

† Electronic supplementary information (ESI) available: Instrument build-up, experimental details, PXRD and Raman images. See DOI: <https://doi.org/10.1039/d4cp04757e>



outcome, generating new products or even inhibiting these reactions.²³ Almost simultaneously, *in situ* monitoring has provided insight into the kinetics and mechanisms of mechanochemical reactions by enabling the measurement of real-time and *in operando* spectroscopic and thermodynamic data without the need for stopping the milling to sample the reaction mixture, which can easily alter the course of the reaction. While indirect methods such as monitoring of the reactor temperature and pressure^{24–26} provided important data for the estimation of mechanochemical reactivity and kinetics, true advancement began with the introduction of direct monitoring techniques, namely synchrotron powder X-ray diffraction (PXRD) reported in 2013²⁷ and laboratory Raman monitoring reported one year later.^{13,28} The two developed methods are highly complementary; PXRD provides insight into the physical evolution of crystalline phases during milling, their particle size,²⁹ and – when combined with a crystalline standard – the quantitative analysis of the occurring amorphous and crystalline phases.³⁰ In turn, Raman spectroscopy provides information about the changes in chemical connectivity and functional groups, regardless of the state of matter of the reaction mixture (gas, liquid, crystalline or amorphous solid), and can even be used as a semi-quantitative tool.³¹ Both techniques reveal the great complexity of mechanochemical reactions, often involving a number of intermediate phases, and also show that these reactions can be surprisingly fast, finishing in a matter of minutes.³² Some of the observed intermediates have already been used in the synthesis of novel advanced materials³³ and the kinetic profiles of certain reactions may be critical for implementing mechanochemistry to industrial processes.^{32,34} *In situ* monitoring of mechanochemical reactions has been so crucial in advancing the field that several monitoring techniques giving different types of insights have recently been developed,^{35–44} often focused on scaled-up mechanochemical processes.^{34,45} However, PXRD and Raman monitoring are still the gold standards for *in operando* monitoring of mechanochemical reactions.

Raman spectroscopy, in particular, is sensitive to the vibrations of the molecular skeleton and offers valuable insight into the breaking and formation of bonds on a molecular level, regardless of the state of matter of the reaction mixture. Thus, unlike PXRD monitoring, it provides insight into the chemical reactivity in amorphous matrices often observed for solid-state organic reactions,⁴⁵ and has detected the formation of supramolecular intermediates that often precede the mechanochemical covalent bond forming.^{46,47} Since the skeleton vibrations are also sensitive to solvation and other intermolecular interactions,^{48,49} Raman spectroscopy may even serve in determining the action of different additives crucial for the success of mechanochemical reactions. Unfortunately, the most commonly used Raman setups in mechanochemistry include fiber-based Raman probes with a spectral resolution of $\sim 10\text{ cm}^{-1}$, so the very small peak shifts for these interactions are often easily overlooked. In addition, these fiber probe setups are expensive, require a high-power beam (up to 500 mW), and often need long exposure times to achieve a sufficiently high signal-to-noise ratio (SNR). This limits the monitoring scope to

thermally stable materials and reactions with relatively slow kinetics and risks missing short-lived intermediates.

To address these challenges, we demonstrate a free-space-optics benchtop Raman device for monitoring mechanochemical reactions built from easily available and affordable commercial parts. We dub it the mechanochemistry Raman System (mcRS). The use of photographic objectives, known for their high light efficiency and excellent aberration correction, enhances the throughput and spectral resolution of the spectrometer. Additionally, by carefully selecting an industrial-grade complementary metal-oxide semiconductor (iCMOS) sensor with low dark noise (DN) and high quantum efficiency (Q_e) at the wavelengths of interest, we achieve an overall sensitivity for mcRS comparable to Raman systems employing scientific-grade charge-coupled device (sCCD) cameras, but at a significantly lower cost. We demonstrate the effectiveness of mcRS on the example of the neat grinding (NG) and the liquid assisted grinding (LAG) synthesis of two different forms of zeolitic imidazolate frameworks (ZIFs) based on zinc and unsubstituted imidazole (HIm). While an ion-and-liquid assisted grinding experiment (ILAG) using ZnO and HIm was previously monitored by *in situ* PXRD,³⁰ to the best of our knowledge this work represents the first example of direct *in situ* Raman monitoring of this system. The mcRS provides kinetic information on the reaction progress and allows the differentiation of two forms of the highly polymorphic zinc imidazolate ZIFs without *in situ* synchrotron PXRD monitoring. It also provides one of the first insights into the interaction of the LAG liquid with the imidazole reagent, and rheological changes during the milling process.

Results and discussion

Mechanochemical Raman system construction

As mentioned, Raman spectroscopy is uniquely qualified to characterise the chemical reactivity in liquid and amorphous matrices, detect the formation of supramolecular intermediates, and determine the action of different additives in mechanochemical synthesis. Monitoring these interactions relies on achieving an excellent spectral resolution of around $4\text{--}7\text{ cm}^{-1}$. Achieving high sensitivity is equally important, as Raman scattering has a cross-section that is 10–12 orders of magnitude smaller than that of molecular absorption, so every photon is important under these low-light conditions.⁵⁰

While research-grade Raman spectrometers (rgRS) achieve even higher resolution, typically around $3\text{--}4\text{ cm}^{-1}$, they come with significant drawbacks, namely their high cost, bulkiness, and the difficulty of coupling their excitation beams to a jar oscillating at 25–35 Hz in a mechanochemical mill. On the other hand, the most commonly used fiber-optic Raman spectrometers (foRS) for *in situ* monitoring have a spectral resolution of around 10 cm^{-1} , meaning they can easily overlook subtle changes in Raman peak shifts. For example, it is hard for them to resolve changes caused by the adsorption of guests on surfaces or into pores of porous materials, which are of huge



importance for the action and applicability of porous coordination materials, such as metal–organic frameworks (MOFs). Additionally, foRS commonly uses 785 nm lasers for excitation, which provides lower sensitivity in the high-frequency range of the Raman spectrum because large Raman shifts push the scattered wavelength further into the near-infrared (around 1 μm), where the sensitivity of silicon-based photodetectors sharply declines. This region contains vital information regarding vibrations, including C–H, O–H, N–H, and other hydrogen-containing bonds. As these bonds are often the basis for hydrogen bonding and other supramolecular interactions of interest, higher sensitivity in this region is crucial. The foRS also require a high-power excitation beam (up to 500 mW) focused on the sample, large slits, and long integration times due to the small number of photons detected on the fiber probe. From our experience, integrations of at least 15–20 s, and slit sizes of 50 μm or more are needed to get satisfactory SNR.

A system offering moderate spectral resolution—between the foRS and the rgRS—and a higher sensitivity compared to the foRS would provide a practical and cost-effective solution for the stated applications. The higher sensitivity would enable the use of shorter integration times while maintaining satisfactory SNR, significantly improving the time resolution of *in situ* monitoring and potentially providing access to short-lived intermediates and insight into the early stages of a mechanochemical reaction.

To address these challenges, inspired by several cost-effective home-built Raman systems used for other applications,^{51–53} we focused on designing an affordable mechanochemical Raman Setup, which is tailor-made to fit the needs of *in situ* and *in operando* monitoring of solid-state synthesis. A schematic of the mcRS including all optical elements along the beam path, starting from the excitation laser and ending at the detector, is shown in Fig. 1. The device can be divided into two parts: the

Raman probe, which focuses the excitation laser inside the jar, collects the Raman scattered photons and couples them at the entrance slit of the spectrometer, and the lens-based dispersive spectrometer that uses an iCMOS camera as detector. The device will be briefly described here, while all the technical details and exact part types are given in the ESI† (Section S1).

Raman probe. For the excitation source, we opted for a single longitudinal mode (SLM) diode laser, which is compact and delivers 50 mW of stable output power at a wavelength of 632.8 nm (L, Fig. 1(A)) and a linewidth of $\Delta\tilde{\nu}_L = 0.4\text{ cm}^{-1}$ (Section S2 in ESI†). Excitation at this wavelength ensures that the whole resulting Raman spectrum ($400\text{--}3500\text{ cm}^{-1}$) falls into the high quantum efficiency region of the Si-based photodetectors (500–800 nm). This enables the excellent sensitivity we require in the high-frequency region, especially compared to the 785 nm excitation lasers commonly used with fiber-based Raman probes. To maintain the high precision necessary for *in situ* mechanochemical experiments, we developed a calibration procedure for the laser source wavelength λ_L (Section S3 in ESI†), which is needed due to the day-to-day variability of λ_L caused by changes in ambient temperature and humidity (approximately $\pm 4\text{ cm}^{-1}$ over one month). Fortunately, simply measuring the spectrum of a Raman shift standard⁵⁴ allows precise determination of the initial λ_L with an uncertainty of $\pm 0.25\text{ cm}^{-1}$, which then remains stable within $\pm 0.05\text{ cm}^{-1}$ during eight hours following the laser switch on, allowing for a full day of data collection without the need for re-calibration.

To shield the laser source from back reflections, a Faraday isolator is inserted immediately after the laser (FI, Fig. 1(A)). The beam is first expanded 2.3 times by a variable magnification beam expander BE. Then, it passes through a laser-line filter F_L . It cleans up all undesired light from the laser or Raman scattering and fluorescence generated in optical elements placed upstream from F_L .

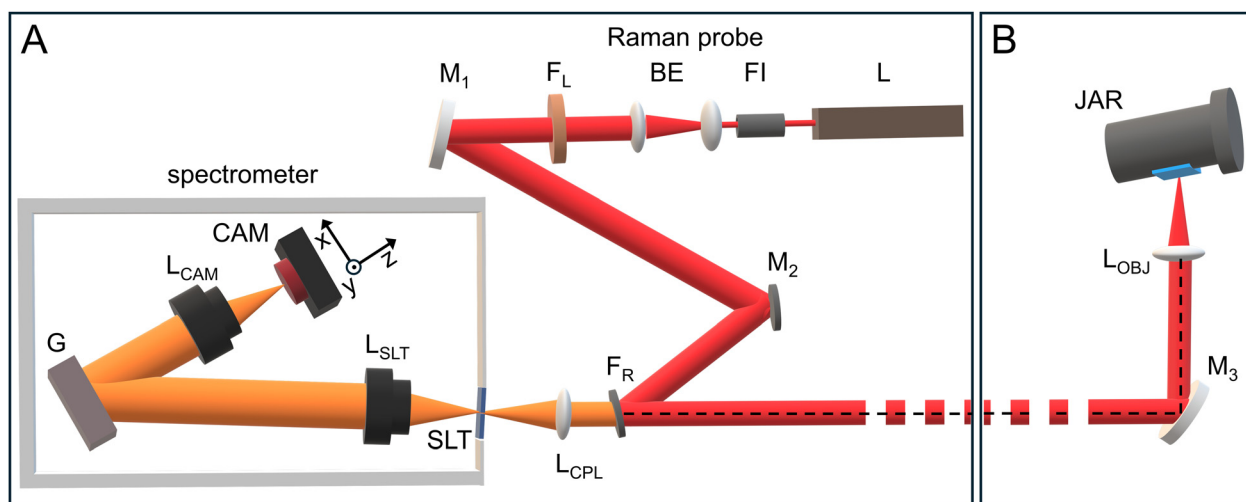


Fig. 1 (A) Scheme of the mechanochemistry Raman System (mcRS), top view: laser L, Faraday isolator FI, beam expander BE, laser filter F_L , Raman edge filter F_R , coupling lens L_{CPL} , entrance slit SLT, slit lens L_{SLT} , diffraction grating G, camera lens L_{CAM} , iCMOS camera CAM. Dashed red line depicts the laser beam that continues up to M_3 ; (B) Side view of the setup in the vicinity of the jar with the vertical folding mirror M_3 , the objective lens L_{OBJ} and the aluminium jar with sapphire window (blue rectangle).



The excitation beam then gets reflected by two folding mirrors (M_1 and M_2) before reaching the long-pass edge filter F_R . As the filter model employed here is an entry-level laser blocking filter, its cutoff wavenumber $\tilde{\nu}_c$ stands at a relatively high value of 350 cm^{-1} . Other filters can (and will be) easily integrated to achieve lower cutoff values. Note that F_R is tilted by 5° relative to the optical axis defined by the objective lens L_{OBJ} and the coupling lens L_{CPL} (Fig. 1(A) and (B), dashed line). This slight tilt allows the excitation beam to be inserted along the optical axis of the Raman probe – in our case, along the L_{OBJ} – L_{CPL} axis – ensuring collinearity between the excitation and Raman-scattered beams. The resulting 2.5° angle of incidence (AOI) induces only a minor reduction of $\tilde{\nu}_c$ by $\sim 6\text{ cm}^{-1}$ compared to the manufacturer's specification, while laser attenuation remains unchanged.

In conventional Raman probe designs, beam collinearity is typically achieved using a dichroic beamsplitter (mounted at an AOI of 45°), followed by a second Raman edge filter at the probe exit to suppress residual Rayleigh scattering. In contrast, our approach eliminates the need for a dichroic beamsplitter and achieves both beam collinearity and Rayleigh suppression using a single long-pass edge filter. This simplified optical layout of the mcRS Raman probe improves throughput, reduces the number of optical components, and lowers the overall cost. Additionally, to the best of our knowledge, it is the simplest design that enables ultralow-frequency (ULF) Raman spectroscopy,⁵⁵ granting access to Raman shifts as low as 5 cm^{-1} .

After it gets reflected on F_R , the excitation beam gets reflected vertically (*i.e.*, perpendicular to the optical plane of the spectrometer) by the last folding mirror M_3 before arriving to the aspheric objective lens L_{OBJ} (Fig. 1(B)), which then focuses the excitation beam on the sample. Choosing an aspheric L_{OBJ} allows us to minimise the spherical aberration that becomes significant for marginal rays and the extensive collection angles necessary to collect as many Raman scattered photons (RSP) as possible and obtain a better SNR. The much larger size of the L_{OBJ} compared to the typical fiber-probe lens also allows for the collection of more RSP and a higher intensity of the measured signal.

For the *in situ* monitoring experiments, we use a 14 mL aluminium jar with sapphire windows described in our previous work,³² positioned so the window points down towards the incoming beam, as most of the reaction mixture is expected to accumulate there during milling.^{13,28} We chose an optical quality sapphire glass window because it is a highly transparent and extremely hard material that can withstand hour-long impacts from stainless steel balls used in the ball-milling process. It shows only two prominent peaks at around 420 and 640 cm^{-1} (easily modelled with a Gaussian curve which makes their removal from the raw Raman spectra straightforward). Conversely, PMMA or poly-(methyl methacrylate), from which most *in situ* monitoring jars are made, shows more than 10 peaks in the region covered by the mcRS.²⁸ Additionally, we subtract the baselines of the empty jar spectrum and of the raw sample spectrum in all experiments. The baseline-corrected empty jar spectrum (Section S4 in ESI†; Fig. S4-2C, red line) is

then normalised to the isolated sapphire peak at 645 cm^{-1} in the baseline-corrected sample spectrum (Fig. S4-2C, ESI† blue line). This allows us to obtain a clean Raman spectrum of the sample, corrected for both the baseline and the jar background (Fig. S4-2D, ESI†).

Lens-based spectrometer. After collection by the L_{OBJ} , the Raman scattered beam is directed into the spectrometer slit by the coupling lens L_{CPL} . Depending on available light, whose amount depends on the Raman scattering efficiency of the sample, the mcRS can easily switch between 10, 15 and $20\text{ }\mu\text{m}$ wide slits. A wider slit generally allows for higher sensitivity, letting through more RSPs, but has a lower spectral resolution, while a narrower slit sacrifices sensitivity in favour of a higher resolution. Extensive testing using a calcite standard (Section S5 in ESI†; Fig. S5-3) shows that although the $10\text{ }\mu\text{m}$ slit offers approximately twice the spectral resolution of the $20\text{ }\mu\text{m}$ slit, achieving comparable SNR requires only 35% longer integration time. This demonstrates that the $10\text{ }\mu\text{m}$ slit provides substantial resolution benefits without a prohibitive increase in acquisition time, offering a good balance between resolution and throughput. All measurements in this work were taken with the $10\text{ }\mu\text{m}$ slit in place.

After the slit, the RSP beam is collimated by a 50 mm photographic objective – the slit lens L_{SLT} on Fig. 1(A) – and directed to a holographic reflective diffraction grating G with the incidence angle $\theta_i = 33.5^\circ$. We keep the grating static while the camera acquires the entire Raman spectrum. Finally, the L_{CAM} focuses the dispersed RSP beam onto the iCMOS camera. We use the same lens as for L_{SLT} . Both lenses in the spectrometer have 50 mm photographic objectives, the most popular lenses in analogue photography for decades. The mass production of the lenses is convenient as one obtains an objective corrected for all optical aberrations in the visible region for less than 300 € .

To acquire the spectra, we opted for an iCMOS camera with a sensor that has a relatively high Q_e (71% at 525 nm), a low RN (2.89 e^- per pixel) and a low dark current (0.8 e^- per s).⁵⁶ With such a slight RN and dark current and for exposures up to $10\text{--}15\text{ s}$, this low-cost, uncooled iCMOS camera will have SNR comparable to an industry-standard sCCD camera cooled by a Peltier element. The extensive usage of the iCMOS camera in our lab has proved that usage of exposures of as large as 20 s is viable without significant image deterioration caused by the thermal noise, even without cooling.

The full details on the protocols for calibration of the wavenumber axis and of the Raman intensity axis, post-acquisition data processing, measurement of the spectral resolution and establishing the laser spot size are all given in the ESI† (Sections S3–S11). In short, it was determined that the free-optics system allows for the use of a narrow $10\text{ }\mu\text{m}$ slit with moderate integration times, resulting in high throughput with an excellent spectral resolution of 7.5 to 4.5 cm^{-1} , depending on the Raman shift $\tilde{\nu}_R$ (Section S5 in ESI†; Fig. S5-1), while the laser spot in the jar has an average FWHM diameter of $2w_j = 8.8\text{ }\mu\text{m}$ (Section S7 in ESI†). The signal intensity scales linearly with sample mass up to approximately 150 mg of imidazole (HIm),



which was determined as the optimal sample mass for the benchmark reaction (Section S12 in ESI†). To maximise the Raman signal, the focal plane of the laser beam needs to be placed around the inner surface of the milling vessel, ideally 0.3–0.5 mm above the sapphire window (Section S14 in ESI†; Fig. S14-1H, dashed line).

Simultaneous sample rheology monitoring. Another unique property of the mcRS is the possibility of monitoring changes in the rheology of the milled reaction mixture. During mechanochemical milling, the physical state of the sample within the jar can undergo significant transformations, evolving from solid particles to fine powder or even into a sticky, glue-like paste that adheres to the jar's walls. It was found that the rheology of the sample may be critical for the chemical reactivity in the jar.⁵⁷ The mechanochemical processing may even be affected by rheology changes if, for example, the milling media is caught up in the viscous material and cannot move inside the milling vessel. In terms of the *in situ* monitoring experiments, this variability in sample rheology poses a unique challenge for *in situ* monitoring techniques, as the changing physical state can affect data acquisition and interpretation. In monitoring experiments, the reduction or the sudden absence of signal often correlates with the changes in rheology of the mixture that got stuck to a localised part of the milling vessel so that it cannot encounter the incident beam. Only stopping the monitoring process may reveal the exact cause, inadvertently interrupting the mechanochemical reaction.

Unlike the foRS, which relies on one-dimensional (1D) line array detectors, we integrated a two-dimensional (2D) image sensor (iCMOS camera) into our mcRS setup. These sensors are not only cost-effective but allow us to acquire a 2D image (the *x*-axis is the wavenumber axis, while the *y*-axis runs parallel to the entrance slit height, Fig. 2(A) inset). The Raman spectrum is then obtained by integrating the columns, *i.e.*, along the *y*-axis, across a range of approximately ± 10 pixels (Section S4 in ESI†; Fig. S4-1, dashed lines) around the line that passes through the maxima of the Raman peaks. It is, however, the width (FWHM) and the shape of the intensity profile of the signal (or of the sample fluorescence), taken along the *y*-axis that can be used to estimate the rheological changes in the milled mixture.

The broadening of the *y*-axis signal is a consequence of the geometry of laser penetration into the sample. As the laser enters the sample, it reaches a focal region before diverging, forming a conical volume of excitation. The observed *y*-axis signal corresponds to the cross-section of this illuminated region when viewed from below through the sapphire window. Thus, the broader the *y*-axis signal, the deeper the laser has penetrated, and the wider the excitation footprint appears (Fig. 2(A), inset).

Several factors influence this broadening: the total amount of sample material, its optical transmittance, and its rheology. A thicker sample allows for a higher maximum number of interacting molecules, but this does not necessarily result in a broader *y*-signal—the laser must be able to penetrate through the sample for broadening to occur. The transmittance of the material dictates how deeply the laser propagates, and thus how many molecules it interacts with. Lastly, even when the

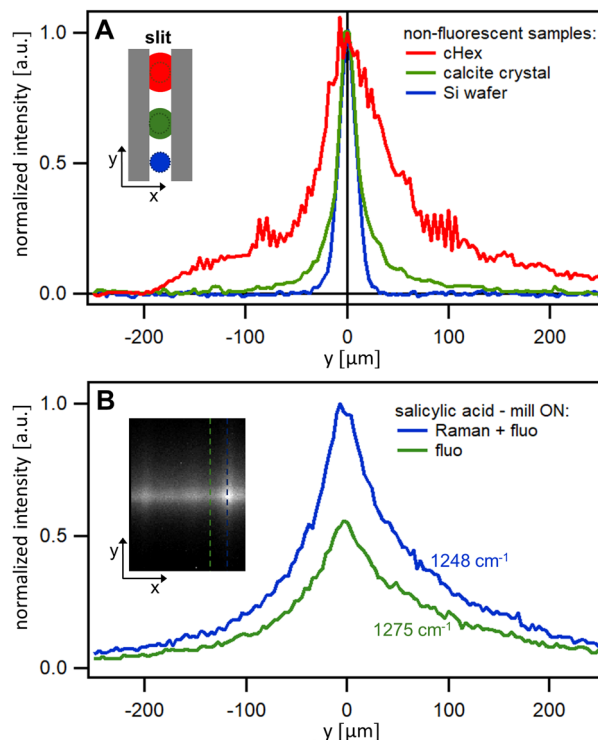


Fig. 2 (A) The Raman signal profile taken along the *y*-axis for an Si wafer (blue), a 0.3 mm thick calcite crystal (green) and cyclohexane liquid (red). The inset illustrates how the excitation footprint increases with penetration depth of the laser and gets imaged on the entrance slit. (B) The Raman signal profiles taken along the *y*-axis for a salicylic acid sample during milling. The blue line is the signal at a Raman peak, while the green line is a pure fluorescence signal. The inset shows an image taken with the iCMOS camera, the dashed lines show where the *y*-axis profiles were taken.

amount of material and its transmittance remain constant, the rheological state of the sample plays a crucial role. A finely dispersed powder provides an open structure in which the laser can travel significant distances and re-scatter, encountering many particles along its path, leading to the broadest *y*-axis signal. In contrast, a dense or sticky material quickly absorbs or scatters the light, limiting penetration and resulting in a narrower signal.

To illustrate these effects, we compare three distinct experimental cases. The first case is a compact solid that has low transmittance at the excitation wavelength, such as a silicon wafer. It presents the narrowest possible *y*-axis signal, as the laser interaction is effectively confined to a two-dimensional surface: a sharp (FWHM = 23 μm), Gaussian-shaped *y*-axis Raman signal at 520 cm^{-1} (Fig. 2(A), blue line) can be observed. This case is analogous to a highly dense reaction mixture that is completely opaque to the excitation beam, such as when the sample becomes stuck to the walls of the milling jar. In the second case, we look at a 0.3 mm thick calcite crystal, which has high transmittance at 633 nm but due to its limited thickness, the total number of laser-sample interactions remains restricted. Here, the *y*-axis signal maintains the same FWHM as silicon but exhibits extended wings that persist up to $\pm 100 \mu\text{m}$ (Fig. 2(A), green line) – the profile acquires a Lorentzian-like shape.



An experimental analogue is a dense slurry or paste that is still mobile (*i.e.*, not “stuck” on the jar walls), where the excitation beam can penetrate several hundred microns into the sample but remains partially confined. Finally, we put a droplet of cyclohexane (>2 mm thick) on the sapphire window, which has both a high transmittance and is thick. The FWHM drastically increases to 75 μm (Fig. 2(A), red line) and again the y-axis signal has notable resemblance to a Lorentzian profile, representing a large number of interactions and a large conical volume of excitation. This simulates a typical mechanochemical reaction where the sample is a polycrystalline powder dispersed throughout the milling vessel. Acquiring images of salicylic acid (SA) as it is milled in the jar shows a y-axis signal profile shape very similar to that of cyclohexane (Fig. 2(B)). Interestingly, due to two-photon absorption, SA demonstrates a weak fluorescence that can also be used to monitor the rheology of the sample. If the y-axis signal is taken at a Raman peak (*e.g.*, at the 1248 cm^{-1} peak of SA), it is the sum of the Raman and the fluorescence contributions (Fig. 2(B), blue line). However, if the y-axis signal is taken where there are no Raman peaks (*e.g.*, at 1275 cm^{-1}), only the fluorescence will contribute to the signal, but the Lorentzian-like shape remains and FWHM can still be estimated, thus the rheology monitoring is still possible. For more details, see Section S14 in ESI.[†]

Comparison of performance of mcRS compared to standard monitoring Raman device. We compared our custom-made mcRS to our in-house foRS, the most often used device for monitoring mechanochemical reactions.²⁸ The foRS consists of an SLM 785 nm laser source from the same manufacturer as the one used in mcRS (USHIO), a BWTek 102B fiber probe, and the OceanOptics MayaPro2000 spectrometer. Using the Raman spectrum of **HIm** under milling conditions (IST500 mill, 30 Hz) as a benchmark, the mcRS shows a significant increase in sensitivity and SNR. This is particularly visible in the high-frequency region, where our choice of laser source, combined with an objective lens with a more extensive collection angle and a 2D detector camera, allows easy detection of the vibrations involving C–H bonds. The traditional foRS cannot resolve these peaks, despite four times longer integration and much

stronger laser power (Fig. 3). Even peaks in the mid-frequency range (*e.g.*, the peaks between 1050 and 1100 cm^{-1} , and the double peak at 1260 cm^{-1} which only shows as a shoulder in the foRS) are significantly better resolved in the mcRS compared to the foRS, under equivalent or lower integration times. The total cost of our device, including the SLM laser source, the iCMOS camera, and all optical components, is five-fold lower compared to a commercial setup and almost half of the price of previous in-house systems (see Section S1 in ESI[†] for a breakdown of the costs). Moreover, the mcRS offers not only higher sensitivity and spectral resolution but also the ability to estimate the rheology of the reaction mixture, and increased modularity and tunability, making it excellent for tailoring to different applications.

A benchmark mechanochemical reaction. A great target for testing the mcRS is the mechanochemical synthesis of ZIFs. ZIFs are 3D-periodic covalently bound frameworks built from tetrahedral metal cations (often Zn^{2+} , Co^{2+} or Cd^{2+}) and imidazolate anions. They are thermally and chemically stable, often highly porous, and have many potential applications as sorbents, catalysts, and in separations.⁵⁸ Due to the linker and metal geometry and connectivity, these materials can – like their zeolite namesakes – form many different arrangements of building blocks in space, called topologies. For example, the simplest of these materials, the unsubstituted zinc imidazolate (**ZnIm**₂) appears in at least 18 different topologies,⁵⁹ presenting one of the most topologically diverse materials known. The targeted synthesis of these different forms is still challenging and generally relies on using solvents as putative templates. Even then, the solvothermal syntheses, which use large amounts of solvents and need to be extensively heated, often provide mixtures of topological products.⁵⁸

Mechanochemical syntheses of ZIFs have many sustainability-based advantages but also provide an avenue for a larger degree of topological control of the reaction outcome. Judicious choice of liquid and ionic solid,^{60–62} or non-ionic solid additives^{22,63} can strongly preference specific product topologies. While the kinetics and yield of these reactions can be monitored by pressure and temperature logging,⁶⁴ as well as *ex situ*⁶⁵ and *in situ* Raman spectroscopy,^{66,67} topological outcomes have so far only been monitored by synchrotron-based *in situ* PXRD.^{27,68} A laboratory-based technique that could provide insight into the topological evolution of ZIF syntheses and simultaneously observe the interaction of the template with the reagents would prove highly advantageous.

We here validate the performance of the mcRS by monitoring the reaction between ZnO and **HIm** under NG and LAG conditions, using ethanol as the LAG additive in the latter case (Fig. 4). The monitoring provides a simple way to differentiate between two topological forms of zinc imidazolate-based ZIF, and shows the interaction of the ethanol liquid additive with the imidazolate linker, along with allowing us to monitor the rheology of the reaction mixture. ZnO and **HIm** were placed in an aluminium milling jar with a sapphire window in a 1 : 2 stoichiometric ratio and two 1.4 g stainless steel ball bearings. In the LAG reaction, 1.67 ethanol equivalents (based on Zn)

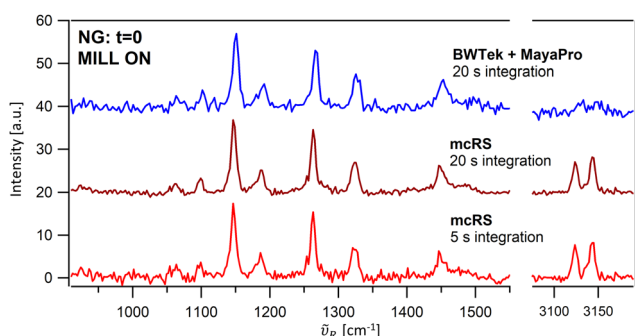


Fig. 3 Comparison of the Raman spectra collected at the beginning of milling of imidazole with the standard fiber-optics Raman system using 20 s integration (blue), and with mcRS using 20 s integration (dark red) and 5 s integration (red). Power of the excitation source: 300 mW for fiber-optics spectrometer and 25 mW for mcRS.



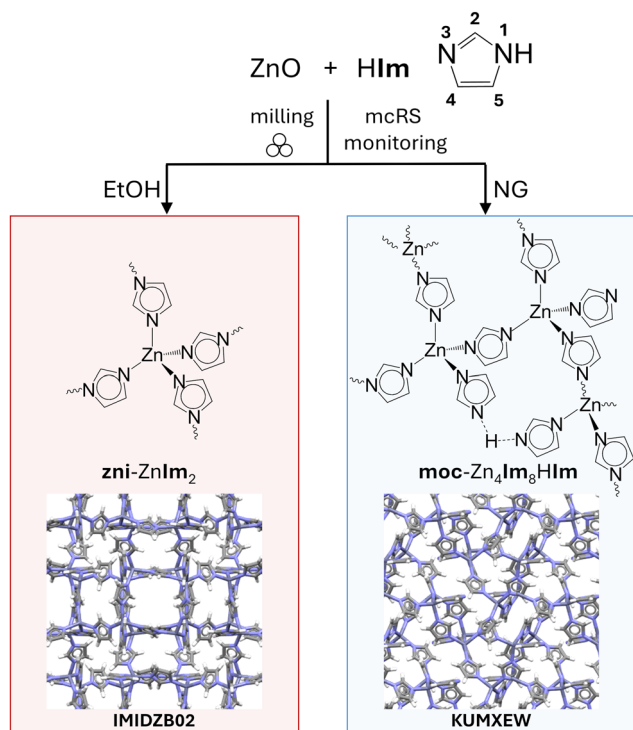


Fig. 4 Schematic representation of the neat (NG) and ethanol assisted mechanochemical reaction between zinc oxide and imidazole, showing the chemical diagrams and images of crystal structures for the products **moc-Zn₄Im₈HIm** (CSD code KUMXEW⁶⁹) and **zni-ZnIm₂** (CSD code IMIDZB02⁷⁰). Labeled molecular diagram of the imidazole molecule.

were added to the mixture. The milling vessel was then placed in the mixer mill and agitated at 30 Hz for up to 90 min, with simultaneous Raman monitoring.

Based on PXRD analysis (Section S15 in ESI†), the NG and ethanol LAG reaction products are **moc-Zn₄Im₈HIm**⁶⁹ and **zni-ZnIm₂**⁷⁰ materials, respectively. Both materials are densely packed three-dimensional coordination polymers of zinc and imidazole (Fig. 4). In the **zni-ZnIm₂** material all imidazole molecules are fully deprotonated (**Im⁻**) and coordinated to zinc cations through both their nitrogen atoms, bridging over two zinc cations each. The zinc cations in turn are tetrahedrally coordinated with four imidazoles each (Fig. 4). The imidazole-bridged zinc cations form four-membered rings that are stacked along the *c*-axis, and interconnected *via* 10-membered rings, building the non-zeolitic **zni** topology. The end result is a highly symmetrical structure adopting the *I*₄*1cd* tetragonal space group, in which many of the imidazolate anions have an identical environment. On the other hand, the **moc-Zn₄Im₈HIm** material has an interrupted non-zeolitic **moc** topology. While the zinc cations are still all tetrahedrally coordinated by imidazoles, one half is surrounded by four fully deprotonated, bridging imidazoles, while the other half is surrounded by three bridging imidazoles, and one terminal imidazole. These terminal imidazoles are so arranged in the structure that they share one proton amongst themselves through hydrogen bonding, making a [**Im**⋯H⋯**Im**]⁺ moiety

(Fig. 4) where these imidazoles are on average half-protonated. While the bridging imidazoles and their zinc cations form four-membered rings similar to those in the **zni-ZnIm₂** structure, they are not interconnected *via* other ring structures, due to the interruption in imidazolate bridging. This results in a structure of much lower symmetry, adopting the *P* $\bar{1}$ space group. Not only does this structure inherently have many different environments the imidazole moieties can inhabit due to its low symmetry, it also contains hydrogen bonding, partial protonation, and different coordination modes for some of the imidazole molecules. This can result in differences in the Raman spectra, which could be used to differentiate these two products.

We will first focus on the Raman monitoring results of the NG reaction, where **moc-Zn₄Im₈HIm** is formed. We observe a relatively slow reaction kinetics (Fig. 5(A)), where the new Raman peaks appear after 2 min, and the reagent peaks largely disappear only after 25 min. Unfortunately, the most diagnostic change for this reaction, namely the deprotonation of the imidazole reagent into the imidazolate ligand, is invisible by Raman spectroscopy. The N–H stretching vibration peak is so broad (3015–2615 cm⁻¹)⁷¹ that is not detectable even by a high-throughput and high-resolution rgRS (Section S16 in ESI†; Fig. S16-1). Instead, the main changes in the reaction mixture Raman spectra result from the coordination of the imidazolate ligands to zinc ions. They consist of the blueshifts of peaks at 1146, 1263, and 1446 cm⁻¹ to their new values of 1174, 1279, and 1488 cm⁻¹, the appearance of new peaks at 975 and 3102 cm⁻¹, and the almost complete disappearance of the peak at 3143 cm⁻¹ (Fig. 5(A)). According to literature,^{71,72} the blue-shifted peaks correspond to in-plane deformation of the C₄,C₅–H bonds and of the ring ($\delta(C_4, C_5-H) + \delta(R)$), the in-plane deformation of the ring ($\delta(R)$), and the combined in-plane deformation of the ring and N₁–H bond ($\delta(R) + \delta(N_1-H)$), respectively. It is, therefore, unsurprising to notice a shift of these peaks to higher frequencies, as the coordination of imidazole rings to zinc ions will naturally constrain the ring motion so that the in-plane deformations will be more difficult and thus higher in energy (and frequency).

Similarly, the new peak at 978 cm⁻¹ corresponds to out-of-plane vibrations of the (C₄,C₅)–H bonds, assigned compared to the Raman spectra of ZIF-8.⁷³ This corresponds to a >40 cm⁻¹ blue shift from the same peak predicted in the starting imidazole spectrum (930 cm⁻¹),⁷¹ which is experimentally of very low intensity and is almost undetectable. Both the coordination of imidazolate to Zn and the proximity of other imidazoles in the densely packed **moc-Zn₄Im₈HIm** structure will limit the motions of these C–H bonds, requiring more energy to initiate them and shift their peak to higher frequencies. The change in intensity of this peak from very weak (undetectable) in imidazole to medium weak in the resulting ZIF likely stems from the change in the protonation state. The deprotonated imidazolate is higher in symmetry, so the out-of-plane vibrations of the (C₄,C₅)–H bonds result in a relatively large change in polarizability and a detectable Raman signal. This has also been demonstrated and assigned in other imidazolate species.⁷⁴



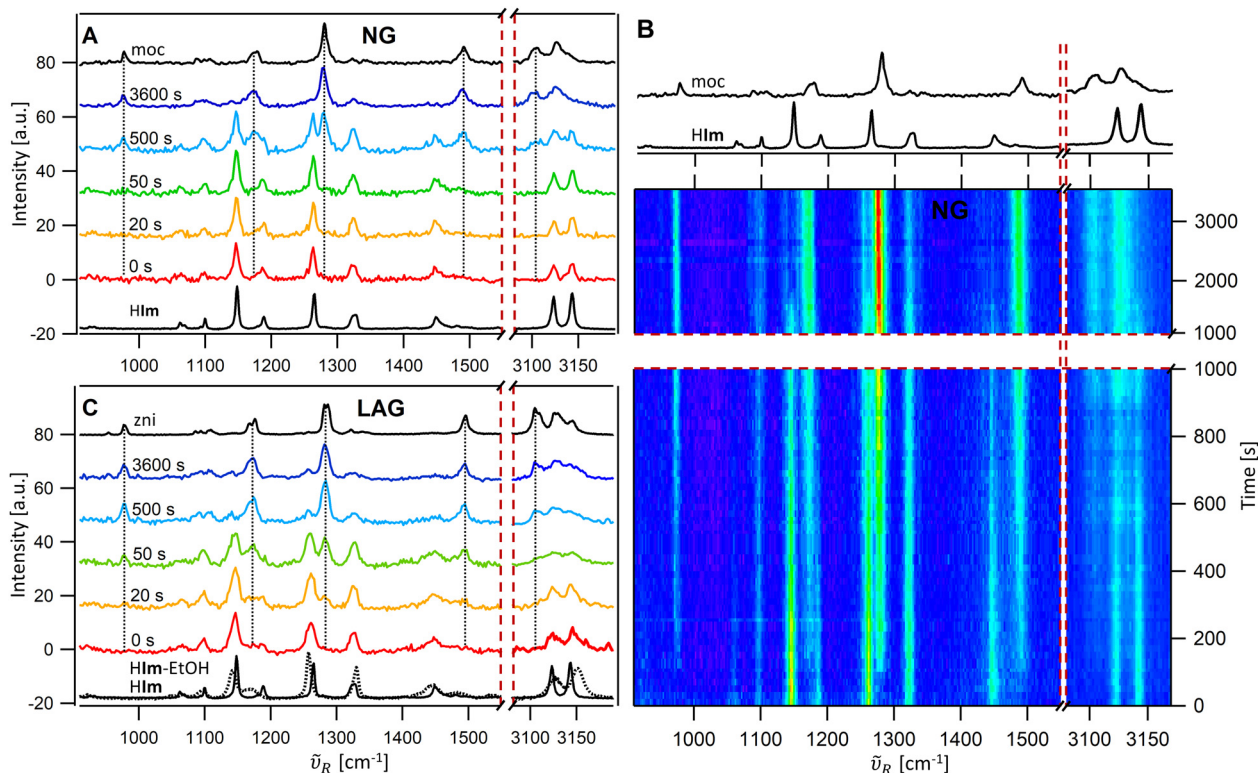


Fig. 5 (A) Time-resolved Raman spectra of the neat grinding (NG) reaction involving ZnO and HIm taken with mcRS. The spectra are displaced vertically for clarity. The dashed vertical lines guide the eye and mark the appearance of the peaks of the **moc** product. The reference spectra of HIm and the **moc** product, taken with a commercial Raman spectrometer, are shown at the top and the bottom of the graph (black line); (B) Waterfall graph for the reaction from A, displaying a total of 75 reaction time points. The red dashed horizontal lines separate the lower and upper panels, which use different time steps: 20 s per step for the lower panel and 100 s per step for the upper panel. This split enables a detailed observation of the reaction kinetics at different time scales. The reference spectra of HIm and the **moc** product are shown above the waterfall plot; (C) As in A, but for LAG reaction with ethanol as the milling additive. The reference spectra of HIm dissolved in EtOH (dashed line, bottom), of HIm (black line, bottom) and of the **zni** product (black line, top) are shown in the top and the bottom of the graph.

Finally, the appearance of a new peak at 3102 cm^{-1} and the near disappearance of the peak at 3143 cm^{-1} both reflect changes in the C–H stretching vibrations. Calculations⁷¹ predict three C–H stretching peaks in imidazole (3140 , 3133 , 3119 cm^{-1}), only two of which (3143 and 3123 cm^{-1}) are of high enough intensity to be measurable in the solid state. This is likely due to both the symmetry of the imidazole molecules, and the way they pack in the solid state (imidazole crystallises in the $P2_1/c$ space group, CSD code: IMAZOL02⁷⁵). During the mechanochemical reaction, imidazole molecules are deprotonated and coordinated to zinc atoms so that both the individual symmetry of the molecules, as well as the overall symmetry of the forming ZIF, are now different than in the parent imidazole. In the case of **moc-Zn₄Im₈HIm** this change of symmetry corresponds to the aforementioned appearance of a new peak at 3104 cm^{-1} and the near disappearance of the peak at 3143 cm^{-1} .

In the LAG reaction, we observe the first difference from the NG reaction before milling is even initiated. Namely, the addition of ethanol to the reaction mixture causes a solvatochromic shift of the Raman peaks of the imidazole reagent. By measuring Raman spectra of HIm in four solvents with varying polarities and proticities (Section S17 in ESI†; Fig. S17-1) we tried to understand origin of the peak shifts in going from the

HIm crystal to a solvated environment. The molar ratio between solute and solvent was kept the same as in the LAG reaction and the following solvents were used: acetonitrile (ACN), dichloromethane (DCM), iso-propanol (iPrOH) and ethanol (EtOH). Almost all major peaks in the fingerprint region show redshift ($5\text{--}30\text{ cm}^{-1}$), except for the ring breathing mode at 1325 cm^{-1} , which undergoes a minor blueshift ($3\text{--}4\text{ cm}^{-1}$), and the C–H stretching modes, which shift slightly to higher frequencies ($4\text{--}9\text{ cm}^{-1}$). No clear correlation was found between these peak shifts and macroscopic solvent parameters^{76–78} (Section S17 in ESI†; Table S17-1), indicating that specific short-range solute–solvent interactions, such as hydrogen bonding, play a major role in solvation of HIm. While a more detailed interpretation could be achieved through molecular dynamics and quantum chemical calculations, as demonstrated by Kumar and coworkers in their study of Raman solvatochromism of benzophenone,⁷⁹ such analysis is beyond the scope of the present study.

The starting spectrum of the ethanol LAG reaction mixture (Fig. 5(C), 0 s red spectrum) is a convolution of the signals of dry imidazole (Fig. 5(C), black bottom spectrum, solid line) and imidazole dissolved in ethanol (Fig. 5(C), black bottom spectrum, dashed line). This strongly implies that part of the



imidazole reagent is solvated (or partially dissolved) by the added ethanol at the beginning of the mechanochemical reaction. To the best of our knowledge, this is the first direct observation of the solvating effect of the liquid additive in a mechanochemical metal–organic framework (MOF) synthesis. Further exploration of this phenomenon could provide crucial insight into the role of liquid additives in mechanochemical MOF syntheses.

Secondly, we can see much faster kinetics than the NG reaction (Fig. 5(C)), wherein the first product peaks appear after only 20 s, and the reaction is nearly complete after 2 minutes. We can monitor the kinetics through the changes in the mid-frequency region of the Raman spectra, which are analogous to those in the NG reaction after the solvatochromic effect has been accounted for. Looking at the high-frequency region, we still observe the appearance of a new peak at 3104 cm^{-1} , similar to the NG reaction. However, the peak at 3150 cm^{-1} does not disappear; instead, we observe a $>50\%$ drop in intensity. This provides an easy way to differentiate the two possible products of this mechanochemical reaction simply by looking at the high-frequency spectral region. The difference is again most likely due to the different symmetry of the products. **zni**- ZnIm_2 ($I4_1cd$, CSD code IMIDZB02⁷⁰) has a much higher symmetry than **moc**- $\text{Zn}_4\text{Im}_8\text{HIm}$ ($P\bar{1}$, CSD code KUMXEW⁶⁹). Any perturbations caused by C–H bond vibrations will, therefore, cause a comparatively larger change in the polarisation of molecules in the highly symmetrical **zni**- ZnIm_2 than in the already low-symmetry **moc**- $\text{Zn}_4\text{Im}_8\text{HIm}$. Since the intensity of Raman signals is proportional to the change of polarizability caused by molecular motion, it is perhaps unsurprising that the highly symmetrical **zni** structure is more affected and thus has more peaks in the high-frequency region. Looking at the high-resolution spectra of the **zni** form (Fig. 6, dark blue line), even more splitting of the peaks can be seen that is not pronounced in the **moc** form.

As mentioned previously, the foRS has a much worse spectral resolution at high frequencies than our mcRS, so it couldn't resolve these minor differences. Instead, the shift of one wide and low-intensity spectral band would be observed, and any chance of differentiating the different forms produced by the reaction of zinc oxide and imidazole would be lost. The unprecedented resolution and sensitivity of our mcRS system thus enables the easy differentiation of the two topological products of ZIF synthesis, solely based on laboratory *in situ* Raman spectroscopy, and emphasises its unique suitability for *in situ* monitoring of mechanochemical ZIF and MOF syntheses.

It is important to note that these two forms display even more distinct differences in the low-frequency region of their spectra (Section S16 in ESI†; Fig. S16-3), corresponding to the differences in their lattice vibrations. In the future, we plan on adapting our mcRS setup to include *in situ* monitoring of this region by simply including appropriate low-wavenumber Raman edge filters ($\sim 900\text{ €}$).

As mentioned before, the shape of the *y*-axis signal, can be used to estimate the rheological changes in the milled mixture. In our experiments, the reaction mixture remained polycrystalline

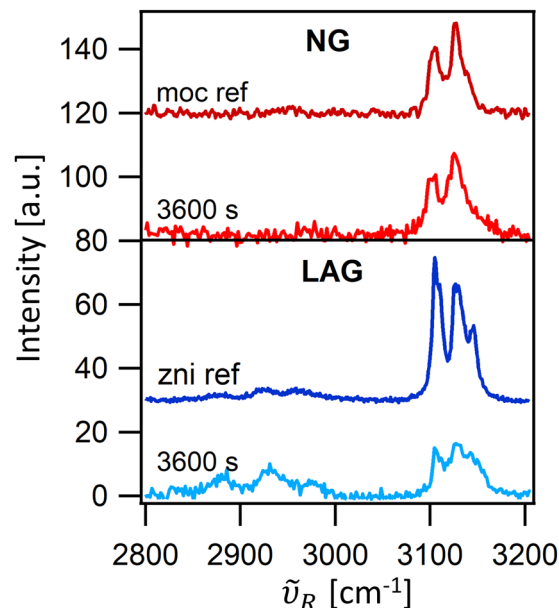


Fig. 6 Raman spectra in high-frequency region of the **moc** product (dark red and red line) and of the **zni** product (dark blue and light blue line): taken *ex situ* with a commercial research grade Raman system (**moc** ref and **zni** ref) and *in situ* with our mechanochemical Raman system at the end of the NG and the LAG reactions (3600 s red and light blue, respectively).

throughout the whole NG experiment (Fig. 7(A) and (B)), as evidenced by the *y*-axis signal's notable resemblance to a Lorentzian profile. This is observed in the wide wings of the profile shape (Fig. 7(A) and (B), red line), or as a “smearing” of the signal in the *y*-dimension (Fig. 7(A) and (B), 2D grayscale images). The minimal changes in rheology are further corroborated by the slight increase in the FWHM of the *y*-axis signal, which broadens only from $100\text{ }\mu\text{m}$ at the start to $125\text{ }\mu\text{m}$ after one hour of milling (Fig. 7(C)).

The LAG experiment initially appears very similar to the NG experiment (Fig. 7(D)), indicating a well-dispersed powder in the milling jar. However, compared to the NG reaction, the FWHM is significantly larger at the start of milling ($290\text{ }\mu\text{m}$), suggesting an even greater dispersion of the powder. This indicates that the ethanol present in the LAG system enhances the initial spread of the particles. In contrast to the NG experiment, the addition of ethanol in the LAG experiment induces a rapid transition from a dispersed powder to a paste, as evidenced by a sharp decrease in the FWHM of the *y*-axis signal to $70\text{ }\mu\text{m}$ at 460 s (Fig. 7(F)). The FWHM then recovers to $\sim 100\text{ }\mu\text{m}$, maintaining this width until 930 s , when it drops again to $\sim 60\text{ }\mu\text{m}$, remaining virtually unchanged until the end of milling. This final sharp profile indicates the formation of a thinner, denser layer on the sapphire window, suggesting that the reaction mixture transformed into a dense paste during the experiment, which also matches our experimental observations when the jar is opened after the reaction is finished. The observed fluctuations in the FWHM present an unresolved aspect of the process, and future investigations will be required to fully understand their origin. To the best of our knowledge, this is the first example of the *in situ* estimation of the rheology



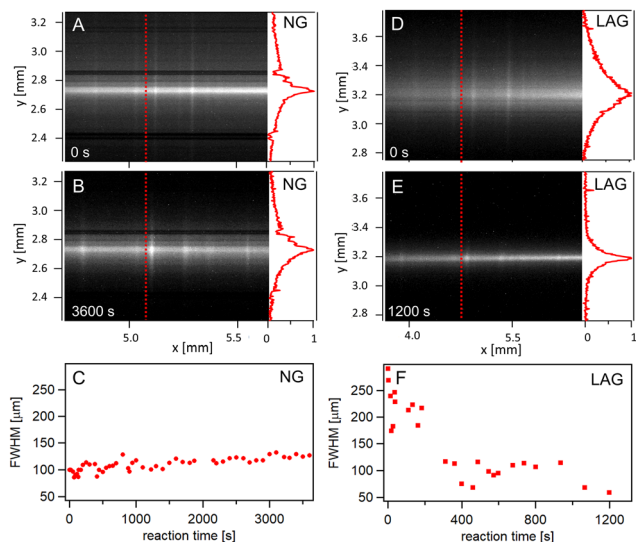


Fig. 7 Monitoring of sample rheology under NG (A)–(C) and LAG conditions (D)–(F) during the reaction between ZnO and HIm. Spectra are shown at the beginning (0 s) and the end of the reaction (3600 s for NG, 1200 s for LAG). The normalized intensity profile along 1300 cm^{-1} (fluorescence signal only, red dashed line) is displayed at the right edge of each spectrometer image section (red line, referred to as the y -axis signal in the text). Panels C and F illustrate the evolution of the FWHM of the y -axis signal throughout the NG and LAG reactions, respectively. The dark horizontal stripes in A and B result from dust particles adhered to the entrance slit.

of a mechanochemical reaction, and it could prove to be an interesting development for the field.

Conclusions

In conclusion, we presented here a custom-made Raman system tailored for the *in situ* monitoring of mechanochemical reactions (the mcRS). Judicious choice of the excitation source, free-space optics, and an iCMOS camera used as a detector provided a cost-effective system with a 30% improvement in spectral resolution and a fivefold improvement in time resolution when compared to fiber-probe Raman systems currently used for *in situ* monitoring of mechanochemical reactions. The mcRS is also highly modular and allows for easy change of the source, slits, and all optical components so that each system can be specifically tailored to the materials and applications researched by an individual laboratory. All this comes at one-fifth of the price compared to the current state-of-the-art commercial setups and one-half of the price of previous in-house fiber optics systems. Additionally, our mcRS allows for estimating the changes in rheology of the sample without stopping the milling or opening the milling vessel. Rheology changes in mechanochemical reactions are a common stumbling block in the scale-up process, and further insight into them could vastly accelerate the commercial use of mechanochemical methods.

The resolution and sensitivity of our mcRS system have proven invaluable in the study of mechanochemical ZIF synthesis. Along with allowing for monitoring the kinetics of their

mechanochemical formation, it enabled the first *in situ* differentiation of two different topological products of ZIF milling synthesis purely based on in-house techniques. This complements the existing PXRD monitoring techniques while lessening the need for expensive, time-consuming and scarcely available synchrotron access. In addition, the spectral resolution of the mcRS system enabled us to directly observe the effect of an additive on the reagents in a LAG mechanochemical reaction, which is still an unresolved issue in the field. The superior sensitivity of free-space optics mcRS might even help elucidate subtle interactions of solid reagents in the initial stages of mechanochemical reactions, such as the association involved in creating hydrogen bonds in cocrystals or even detecting preorganisation of reagents that template molecules can provide through intermolecular interactions. The 2D imaging achieved through the iCMOS camera enabled us to monitor the rheology of the milled reaction mixture in real time, showing crucial differences between the NG and LAG reactions.

We are currently expanding the applicability of the setup by using low-wavenumber Raman edge filters, which will allow us to monitor the low-frequency part of the Raman spectrum ($25\text{--}350\text{ cm}^{-1}$), where the collective modes of framework vibrations are particularly accentuated. We also plan to apply the mcRS to different types of mechanochemical reactions in order to gain insight into the still unresolved mechanisms by which liquid additives accelerate and direct mechanochemical reactivity.

Author contributions

GZ – writing – original draft, writing – review & editing, visualization, conceptualization, investigation, supervision. AS – Investigation. NV – software. KU – funding acquisition, writing – review & editing, conceptualisation. DČ – conceptualisation, methodology, investigation. IB – funding acquisition, writing – original draft, writing – review & editing, visualisation, conceptualisation, investigation. MR – funding acquisition, visualisation, supervision, writing – editing.

Data availability

All data produced and analysed in this study are available in the published article and its ESI,[†] as well as on the Zenodo archive: <https://doi.org/10.5281/zenodo.14503557>. The software used for data analysis can be found at: <https://doi.org/10.5281/zenodo.14479272>.

Conflicts of interest

There are no conflicts to declare.

Acknowledgements

The work has been supported in part by the “Research Cooperability” Program of the Croatian Science Foundation from the



European Social Fund under the Operational Programme Efficient Human Resources 2014-2020 (grant PZS-2019-02-4129), and by the Croatian Science Foundation (grant IP-2020-02-4702). This work has also been supported by the “Developing Research Support” Program of the Croatian Ministry of Science and the Croatian Science Foundation, funded by the European Union from the NextGenerationEU programme (grant NPOO.C3.2.R2-I1.06.0049). We acknowledge the support of the project *Compact Raman device with advanced features* NPOO.C3.2.R3-I1.02.0005 financed by the European Union through the National Recovery and Resilience Plan 2021–2026. This work was also supported by the project Centre for Advanced Laser Techniques (CALT), co-funded by the European Union through the European Regional Development Fund under the Competitiveness and Cohesion Operational Programme (grant no. KK.01.1.1.05.0001).

Notes and references

- 1 K. J. Ardila-Fierro and J. G. Hernández, *ChemSusChem*, 2021, **14**, 2145.
- 2 S. L. James, C. J. Adams, C. Bolm, D. Braga, P. Collier, T. Friščić, F. Grepioni, K. D. M. Harris, G. Hyett, W. Jones, A. Krebs, J. Mack, L. Maini, A. G. Orpen, I. P. Parkin, W. C. Shearouse, J. W. Steed and D. C. Waddell, *Chem. Soc. Rev.*, 2012, **41**, 413.
- 3 D. Braga, L. Maini and F. Grepioni, *Chem. Soc. Rev.*, 2013, **42**, 7638.
- 4 M. Solares-Briones, G. Coyote-Dotor, J. C. Pérez-Franco, M. R. Zermelo-Ortega, C. M. de la O. Contreras, D. Canseco-González, A. Avila-Sorrosa, D. Morales-Morales and J. M. Germán-Acacio, *Pharmaceutics*, 2021, **13**, 790.
- 5 G. W. Wang, *Chem. Soc. Rev.*, 2013, **42**, 7668.
- 6 T. Stolar and K. Užarević, *CrystEngComm*, 2020, **22**, 4511–4525.
- 7 S. B. Peh, Y. Wang and D. Zhao, *ACS Sustainable Chem. Eng.*, 2019, **7**, 3647.
- 8 E. V. Shaw, A. M. Chester, G. P. Robertson, C. Castillo-Blas and T. D. Bennett, *Chem. Sci.*, 2024, **15**, 10689.
- 9 E. Boldyreva, *Chem. Soc. Rev.*, 2013, **42**, 771–7738.
- 10 J. Andersen and J. Mack, *Green Chem.*, 2018, **20**, 1435.
- 11 I. Z. Hlova, S. Gupta, J. F. Goldston, T. Kobayashi, M. Pruski and V. K. Pecharsky, *Faraday Discuss.*, 2014, **170**, 137.
- 12 Y. Sim, Y. X. Shi, R. Ganguly, Y. Li and F. García, *Chem. – Eur. J.*, 2017, **23**, 11279.
- 13 D. Gracin, V. Štrukil, T. Friščić, I. Halasz and K. Užarević, *Angew. Chem., Int. Ed.*, 2014, **53**, 6193.
- 14 G. Ayoub, B. Karadeniz, A. J. Howarth, O. K. Farha, I. Lilić, L. S. Germann, R. E. Dinnebier, K. Užarević and T. Friščić, *Chem. Mater.*, 2019, **31**, 5494.
- 15 V. Martinez, T. Stolar, B. Karadeniz, I. Brekalo and K. Užarević, *Nat. Rev. Chem.*, 2022, **7**, 51.
- 16 F. Gomollón-Bel, *Chem. Int.*, 2019, **41**, 12.
- 17 T. Friščić, S. L. Childs, S. A. A. Rizvi and W. Jones, *CrystEngComm*, 2009, **11**, 418.
- 18 N. Shan, F. Toda and W. Jones, *Chem. Commun.*, 2002, 2372.
- 19 K. Kubota, T. Seo and H. Ito, *Faraday Discuss.*, 2023, **241**, 104.
- 20 D. Hasa, E. Carlino and W. Jones, *Cryst. Growth Des.*, 2016, **16**, 1772.
- 21 T. Friščić, D. G. Reid, I. Halasz, R. S. Stein, R. E. Dinnebier and M. J. Duer, *Angew. Chem., Int. Ed.*, 2010, **49**, 712.
- 22 I. Brekalo, C. M. Kane, A. N. Ley, J. R. Ramirez, T. Friščić and K. T. Holman, *J. Am. Chem. Soc.*, 2018, **140**, 10104.
- 23 M. Arhangelskis, D. K. Bučar, S. Bordignon, M. R. Chierotti, S. A. Stratford, D. Voinovich, W. Jones and D. Hasa, *Chem. Sci.*, 2021, **12**, 3264.
- 24 K. Užarević, V. Štrukil, C. Mottillo, P. A. Julien, A. Puškarić, T. Friščić and I. Halasz, *Cryst. Growth Des.*, 2016, **16**, 2342.
- 25 I. Brekalo, W. Yuan, C. Mottillo, Y. Lu, Y. Zhang, J. Casaban, K. T. Holman, S. L. James, F. Duarte, P. A. Williams, K. D. M. Harris and T. Friščić, *Chem. Sci.*, 2020, **11**, 2141.
- 26 S. Grätz, D. Beyer, V. Tkachova, S. Hellmann, R. Berger, X. Feng and L. Borchardt, *Chem. Commun.*, 2018, **54**, 5307.
- 27 T. Friščić, I. Halasz, P. J. Beldon, A. M. Belenguer, F. Adams, S. A. J. Kimber, V. Honkimäki and R. E. Dinnebier, *Nat. Chem.*, 2012, **5**, 66.
- 28 S. Lukin, K. Užarević and I. Halasz, *Nat. Protoc.*, 2021, **16**, 3492.
- 29 L. S. Germann, A. D. Katsenis, I. Huskić, P. A. Julien, K. Užarević, M. Etter, O. K. Farha, T. Friščić and R. E. Dinnebier, *Cryst. Growth Des.*, 2020, **20**, 49.
- 30 I. Halasz, T. Friščić, S. A. J. Kimber, K. Užarević, A. Puškarić, C. Mottillo, P. Julien, V. Štrukil, V. Honkimäki and R. E. Dinnebier, *Faraday Discuss.*, 2014, **170**, 203.
- 31 S. Lukin, T. Stolar, M. Tireli, M. V. Blanco, D. Babić, T. Friščić, K. Užarević and I. Halasz, *Chem. – Eur. J.*, 2017, **23**, 13941.
- 32 I. Brekalo, V. Martinez, B. Karadeniz, P. Orešković, D. Drapanauskaite, H. Vriesema, R. Stenekes, M. Etter, I. Dejanović, J. Baltrusaitis and K. Užarević, *ACS Sustainable Chem. Eng.*, 2022, **10**, 6743.
- 33 T. Stolar, A. Prašnikar, V. Martinez, B. Karadeniz, A. Bjelić, G. Mali, T. Friščić, B. Likozar and K. Užarević, *ACS Appl. Mater. Interfaces*, 2021, **13**, 3070.
- 34 N. Y. Gugin, J. A. Villajos, O. Dautain, M. Maiwald and F. Emmerling, *ACS Sustainable Chem. Eng.*, 2023, **11**, 5175.
- 35 P. F. M. de Oliveira, A. A. L. Michalchuk, A. G. Buzanich, R. Bienert, R. M. Torresi, P. H. C. Camargo and F. Emmerling, *Chem. Commun.*, 2020, **56**, 10329.
- 36 A. A. L. Michalchuk and F. Emmerling, *Angew. Chem., Int. Ed.*, 2022, **61**, e202117270.
- 37 T. H. Borchers, F. Topić, M. Arhangelskis, M. Ferguson, C. B. Lennox, P. A. Julien and T. Friščić, *Chem*, 2025, **11**(2), 102319.
- 38 T. Friščić, I. Halasz, P. J. Beldon, A. M. Belenguer, F. Adams, S. A. J. Kimber, V. Honkimäki and R. E. Dinnebier, *Nat. Chem.*, 2013, **5**, 66.
- 39 I. Halasz, T. Friščić, S. A. J. Kimber, K. Užarević, A. Puškarić, C. Mottillo, P. Julien, V. Štrukil, V. Honkimäki and R. E. Dinnebier, *Faraday Discuss.*, 2014, **170**, 203.
- 40 S. Lukin, K. Užarević and I. Halasz, *Nat. Protoc.*, 2021, **16**, 3492.



- 41 S. Lukin, T. Stolar, M. Tireli, M. V. Blanco, D. Babić, T. Frišćić, K. Užarević and I. Halasz, *Chem. – Eur. J.*, 2017, **23**, 13941.
- 42 K. Užarević, I. Halasz and T. Frišćić, *J. Phys. Chem. Lett.*, 2015, **6**, 4129.
- 43 Y. Xu, L. Champion, B. Gabidullin and D. L. Bryce, *Chem. Commun.*, 2017, **53**, 9930.
- 44 I. d. A. A. Silva, E. Bartalucci, C. Bolm and T. Wiegand, *Adv. Mater.*, 2023, **35**, 2304092.
- 45 K. J. Ardila-Fierro, S. Lukin, M. Etter, K. Užarević, I. Halasz, C. Bolm and J. G. Hernández, *Angew. Chem., Int. Ed.*, 2020, **59**, 13458.
- 46 T. Stolar, J. Alić, G. Talajić, N. Cindro, M. Rubčić, K. Molčanov, K. Užarević and J. G. Hernández, *Chem. Commun.*, 2023, **59**, 13490.
- 47 S. Lukin, M. Tireli, I. Lončarić, D. Barišić, P. Šket, D. Vrsaljko, M. di Michiel, J. Plavec, K. Užarević and I. Halasz, *Chem. Commun.*, 2018, **54**, 13216.
- 48 A. D. Buckingham, *Trans. Faraday Soc.*, 1960, **56**, 753.
- 49 C. R. Baiz, B. Błasiak, J. Bredenbeck, M. Cho, J. H. Choi, S. A. Corcelli, A. G. Dijkstra, C. J. Feng, S. Garrett-Roe, N. H. Ge, M. W. D. Hanson-Heine, J. D. Hirst, T. L. C. Jansen, K. Kwac, K. J. Kubarych, C. H. Londergan, H. Maekawa, M. Reppert, S. Saito, S. Roy, J. L. Skinner, G. Stock, J. E. Straub, M. C. Thielges, K. Tominaga, A. Tokmakoff, H. Torii, L. Wang, L. J. Webb and M. T. Zanni, *Chem. Rev.*, 2020, **120**, 7152.
- 50 D. Polli, V. Kumar, C. M. Valensise, M. Marangoni and G. Cerullo, *Laser Photonics Rev.*, 2018, **12**, 1800020.
- 51 X. Wang, Y. Yu, Y. Dai, Q. Xu, K. Chu and Z. J. Smith, *IEEE J. Sel. Top. Quantum Electron.*, 2023, **29**, 1–7.
- 52 Y. C. Cho and S. Il Ahn, *Sci. Rep.*, 2020, **10**, 11692.
- 53 C. Mohr, C. L. Spencer and M. Hippler, *J. Chem. Educ.*, 2010, **87**, 326–330.
- 54 A. Ntziouni, J. Thomson, I. Xiarchos, X. Li, M. A. Bañares, C. Charitidis, R. Portela and E. Lozano Diz, *Appl. Spectrosc.*, 2022, **76**, 747.
- 55 M. L. Lin, F. R. Ran, X. F. Qiao, J. B. Wu, W. Shi, Z. H. Zhang, X. Z. Xu, K. H. Liu, H. Li and P. H. Tan, *Rev. Sci. Instrum.*, 2016, **87**, 053122.
- 56 FLIR, 2022 Camera Sensor Review, last accessed on January 30 2025, <https://www.flir.com/landing/iis/machine-vision-camera-sensor-review/>.
- 57 B. P. Hutchings, D. E. Crawford, L. Gao, P. Hu and S. L. James, *Angew. Chem., Int. Ed.*, 2017, **56**, 15252.
- 58 K. S. Park, Z. Ni, A. P. Côté, J. Y. Choi, R. Huang, F. J. Uribe-Romo, H. K. Chae, M. O'Keeffe and O. M. Yaghi, *Proc. Natl. Acad. Sci. U. S. A.*, 2006, **103**, 10186.
- 59 X. Li, Y. Tan, Z. Ju, W. Wang and D. Yuan, *Inorg. Chem. Front.*, 2025, **12**, 701.
- 60 P. J. Beldon, L. Fábrián, R. S. Stein, A. Thirumurugan, A. K. Cheetham and T. Frišćić, *Angew. Chem., Int. Ed.*, 2010, **49**, 9640.
- 61 C. Mottillo, Y. Lu, M. H. Pham, M. J. Cliffe, T. O. Do and T. Frišćić, *Green Chem.*, 2013, **15**, 2121.
- 62 M. J. Cliffe, C. Mottillo, R. S. Stein, D. K. Bučar and T. Frišćić, *Chem. Sci.*, 2012, **3**, 2495.
- 63 I. Brekalo, D. E. Deliz, C. M. Kane, T. Frišćić and K. Travis Holman, *Molecules*, 2020, **25**, 633.
- 64 I. Brekalo, W. Yuan, C. Mottillo, Y. Lu, Y. Zhang, J. Casaban, K. T. Holman, S. L. James, F. Duarte, P. A. Williams, K. D. M. Harris and T. Frišćić, *Chem. Sci.*, 2020, **11**, 2141.
- 65 X. Ma, W. Yuan, S. E. J. Bell and S. L. James, *Chem. Commun.*, 2014, **50**, 1585.
- 66 N. Y. Gugin, J. A. Villajos, O. Dautain, M. Maiwald and F. Emmerling, *ACS Sustainable Chem. Eng.*, 2023, **11**, 5175.
- 67 L. Batzdorf, F. Fischer, M. Wilke, K. J. Wenzel and F. Emmerling, *Angew. Chem., Int. Ed.*, 2015, **54**, 1799.
- 68 A. D. Katsenis, A. Puškarić, V. Štrukil, C. Mottillo, P. A. Julien, K. Užarević, M.-H. H. Pham, T.-O. O. Do, S. A. J. J. Kimber, P. Lazić, O. Magdysyuk, R. E. Dinnebier, I. Halasz and T. Frišćić, *Nat. Commun.*, 2015, **6**, 6662.
- 69 G. A. V. Martins, P. J. Byrne, P. Allan, S. J. Teat, A. M. Z. Slawin, Y. Li and R. E. Morris, *Dalton Trans.*, 2010, **39**, 1758.
- 70 E. C. Spencer, R. J. Angel, N. L. Ross, B. E. Hanson and J. A. K. Howard, *J. Am. Chem. Soc.*, 2009, **131**, 4022.
- 71 L. Colombo, P. Bleckmann, B. Schrader, R. Schneider and T. Plessner, *J. Chem. Phys.*, 1974, **61**, 3270.
- 72 S. Salama and T. G. Spiro, *J. Am. Chem. Soc.*, 1978, **100**, 1105.
- 73 K. I. Hadjiivanov, D. A. Panayotov, M. Y. Mihaylov, E. Z. Ivanova, K. K. Chakarova, S. M. Andonova and N. L. Drenchev, *Chem. Rev.*, 2021, **121**, 1286.
- 74 S. Hashimoto, K. Ono, H. Takeuchi and I. Harada, *Spectrochim. Acta, Part A*, 1994, **50**, 1647.
- 75 Y. A. Omelchenko and Y. D. Kondrashev, *Kristallografiya*, 1971, **16**, 115.
- 76 C. Reichardt, *Pure Appl. Chem.*, 1982, **54**, 1867.
- 77 W. Liptay, *Angew. Chem., Int. Ed. Engl.*, 1969, **8**, 177.
- 78 C. Reichardt, *Angew. Chem., Int. Ed. Engl.*, 1965, **4**, 29.
- 79 V. R. Kumar, C. Verma and S. Umapathy, *J. Chem. Phys.*, 2016, **144**, 064302.

